Rapidly Solidified P/M X2020 Aluminum Alloys

SHINHOO KANG and NICHOLAS J. GRANT

X2020 aluminum alloys were produced with variations in the Li/Cu ratio by the ultrasonic gas atomization process. In alloy 68 (Al-4.9Cu-1.2Li) and 69 (Al-4.4Cu-1.55Li) alloys, the θ' and T_1 phases are dominant with evidence of the T_B phase. In the 70 (Al-3.5Cu-2.8Li) alloy, the δ' phase is dominant with a trace of T_1. It was found that θ' and T_1 are effective strengtheners whereas δ' provides excellent fatigue crack initiation resistance. Overall results indicate that the fracture behavior of three RS-PM X2020 alloys is closely related to alloy production route as well as to the phases present in the alloys.

I. INTRODUCTION

WITH growing demands for improved high strength, low density aluminum alloys for aerospace applications, Al-Li alloys continue to receive research attention.[1,2,3] It has been shown that lithium additions to aluminum alloys result in improved properties such as strength, elastic modulus, (lower) density, fatigue, and stress corrosion resistance; however, lower than anticipated fracture toughness values have delayed commercial use. The low fracture toughness has been attributed to the presence of a high volume of the coherent, ordered δ' phase (Al_3Li) and to weak grain boundary areas caused by precipitate free zones (PFZ) and grain boundary precipitates. Some Al-Cu-Li alloys have demonstrated excellent mechanical properties based on a high volume fraction of fine, secondary phases present in the more highly alloyed materials. Fracture toughness of RS-PM Al-Cu-Li alloys, however, has not been outstanding.

In the present study three X2020 type aluminum alloys with different copper to lithium ratios were chosen and prepared by an ultrasonic inert gas atomization process (USGA), with solidification rates of 10^4 to 10^5 K/s. An effort was made to gain a better understanding of the role of processing variables on the microstructure and mechanical properties of these X2020 alloys. Microstructural analyses were made using transmission electron microscopy and related to the mechanical behavior of the alloys.

II. EXPERIMENTAL

Three master alloys, received as high purity remelt stock from the Reynolds Metals Co., were atomized by an ultrasonic gas atomization process (USGA). The powders, finer than 250 μm in diameter, were screened, canned, evacuated, and consolidated at 400 °C (673 K) with a 30 to 1 extrusion ratio to produce a bar of rectangular cross section: 3.81 × 1.27 cm (1.5″ × 0.5″). The final compositions of the alloys are shown in Table I. Details of alloy preparation can be found in Reference 4. The heat treatments and the evaluation of the structures and mechanical properties of the alloys were based on the derived aging curves.

For studies of the microstructures thin areas were prepared using a Fischione dual jet polishing unit. The electrolyte consisted of 1 part nitric acid and 3 parts methanol. Optimum results were obtained at −40 °C (233 K) with a 40 V potential difference. The prepared samples were examined in a Philips EM 300 electron microscope.

Room-temperature tensile properties were measured using an Instron machine operated at a strain rate of 0.25 mm/min. Reversed bending fatigue tests were conducted on a Wiedeman Universal fatigue machine (Model SF-2-U) to produce S-N curves. The stress ratio used throughout the testing was −1. Specimens for compact tests and fatigue crack growth rate (FCGR) measurements were tested on an MTS hydraulic testing machine (Model 810) according to ASTM Specification E399 and E647. FCGR values of the alloys were measured at 25 Hz with $R = 0.10$ and 0.33.

III. RESULTS AND DISCUSSION

A. *Microstructures of the Alloys*

The microstructures of the three RS-PM Al-Cu-Li alloys were examined after the alloys had been heat treated at optimum aging conditions.[5] Because of the coexistence of many phases in the Al-Cu-Li system,[6] careful distinctions were made between phases by constructing (or computing) the electron diffraction patterns for the phases of interest on the basis of their structures and orientation relationships with the aluminum matrix.

Figure 1 shows the diffraction patterns in Z = [001] and Z = [211] for the phases commonly seen in the Al-Cu-Li system. For the θ' phase, a modified Preston's structure of θ' was used to construct the diffraction patterns.[7,8] Details on the construction of the diffraction patterns of the θ' phase, as an example, are presented in the Appendix. With these considerations, the phases existing in alloys 68-T6, 69-T7, and 70-T6 were differentiated.

Figure 2 shows a typical TEM micrograph (BF) of alloy 68-T6 with a selected area diffraction (SAD) pattern (Z = [001]), confirming the existence of the θ' phase and the modified Preston's structure of θ'. Schneider and Heimendahl[9] indexed a pattern of Z = [001] for the θ' phase in I/M X2020 alloy and considered the appearance of the forbidden θ' reflections in the pattern as a result of the

SHINHOO KANG, formerly Research Assistant, Massachusetts Institute of Technology, is Senior Member of Technical Staff with GTE Laboratories Incorporated, Waltham, MA 02254. NICHOLAS J. GRANT is Professor, Department of Materials Science and Engineering, Massachusetts Institute of Technology, Cambridge, MA 02139.

Manuscript submitted April 1, 1984

Table I. Final Compositions of As-Extruded RS-P/M Alloys (Wt Pct)

Alloy Designation†	Cu	Li	Mn	Cd	Mg	Zn	Fe	Si	Al
2020-68	4.93	1.19	0.39	0.11	0.013	0.015	0.22	0.06	bal
2020-69	4.40	1.55	0.38	0.15	0.031	0.013	0.17	0.06	bal
2020-70	3.53	2.79	0.44	0.19	ND*	ND*	ND*	ND*	bal

ND* = Not determined
† = Each alloy will be referred to as alloys 68, 69, and 70, respectively.

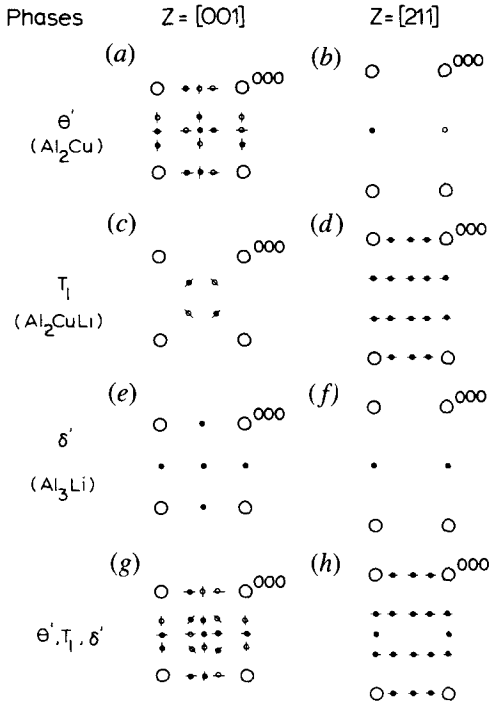

Fig. 1—The diffraction patterns of the θ', T_1, and δ' phases. ○: matrix, ●: precipitates, ○: double diffraction, –: streak.

presence of cadmium in the system. However, the appearance of the reflections was better explained by double diffraction effects of the electron beams as shown in Figure 1. It is common that each diffracted beam in the crystal behaves to some extent as an incident beam and can diffract electrons to a point on the diffraction pattern forbidden by structure factor rules.[10,11] The same double diffraction effect was found in the SAD pattern of the T_1 phase.[12,13]

With the same approach, θ'' can be differentiated from the θ' phase. The streaks around the matrix reflections resulted from the presence of the θ'' phase and can be explained not only by a disc-shaped morphology of the precipitate, but by reflection spots of θ'' which appear in the vicinity of the matrix spots.

Figures 3 and 4 show the bright-field, SAD pattern with a zone axis [211], and the dark-field micrographs obtained using selected reflections of the T_1 phase. Figure 4(a, b, and c) was obtained using reflection spots 'a', 'b', and 'c' in Figure 3(c), respectively. According to Figure 1(b) and (f), Figure 4(b) is due to the θ' and the δ' phases; however, based on precipitate morphology, the precipitate in Figure 4(b) looks more like θ' (50 Å in thickness, 500 Å in diameter) rather than δ' (100 Å in size before coarsening).[14] The δ' phase, in the 70-T6 alloy, will be shown to be in the range of 100 to 200 Å in diameter. Figure 4(c) is a projection of thin hexagonal-shaped platelets of the T_1 phase on the (211) plane; the zone axis for this area is [211] and the habit plane of the T_1 phase is {111}.[12] The 68 alloy showed a high volume fraction of the θ' and T_1 phases throughout the system with PFZ's along the grain boundaries. The δ' phase, which was observed only after solution heat treatment at 525 °C (798 K), did not become a major precipitate in this alloy. The T phase ($Al_{20}Cu_2Mn_3$), of about 0.2 μm particle size, was frequently found intragranularly.

The 69 alloy in the T7 condition shows very similar microstructures to those for the 68 alloy in the T6 condition except for different volume fractions of the dominant phases (Figure 5). It is observed from both alloys that the θ' and T_1 phases dominate over other phases, implying that these phases are responsible for the observed strengthening and the matrix deformation. Differences between the 68 and 69 alloys (Figures 2, 3, and 5) are that the 69 alloy (4.4 pct Cu,

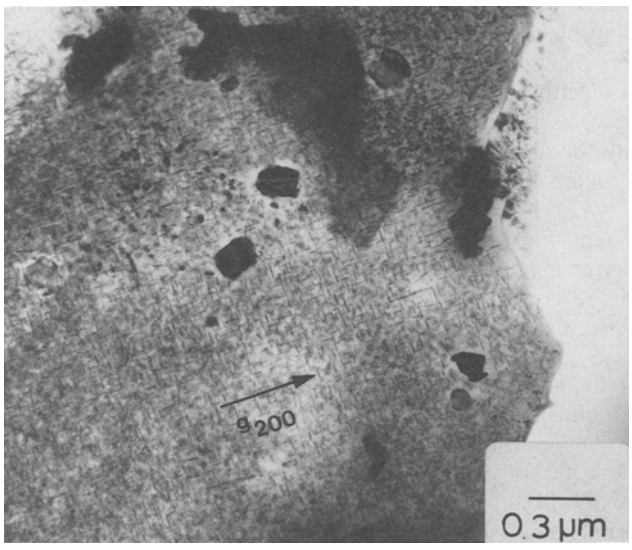

(a)

(b)

Fig. 2—TEM micrograph of 68-T6 alloy: (*a*) BF showing θ' of needle shape and (*b*) SAD pattern of (a) with Z = [001].

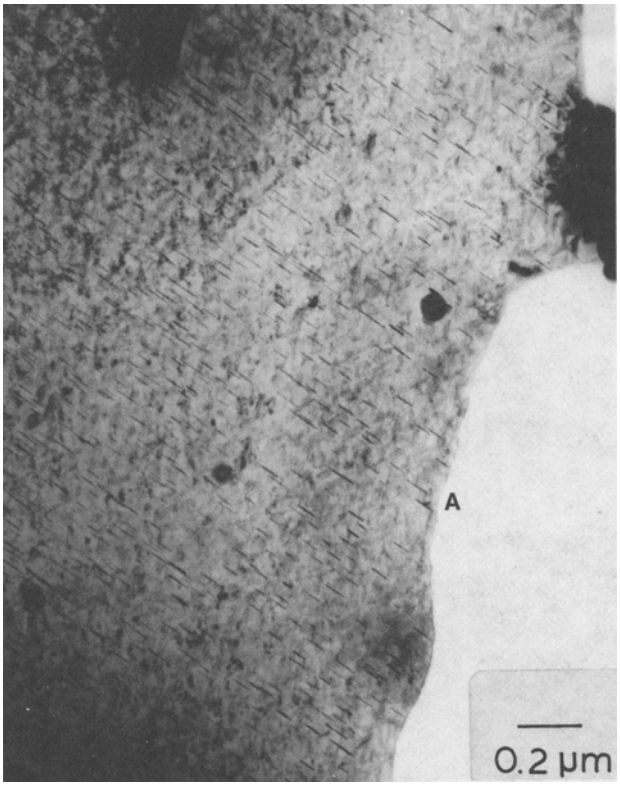

(a)

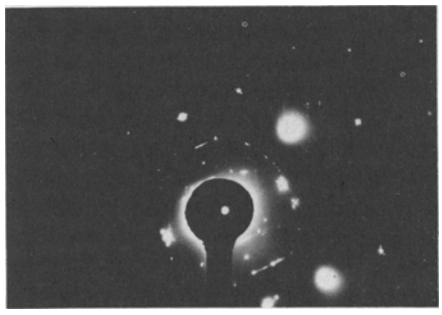

(b)

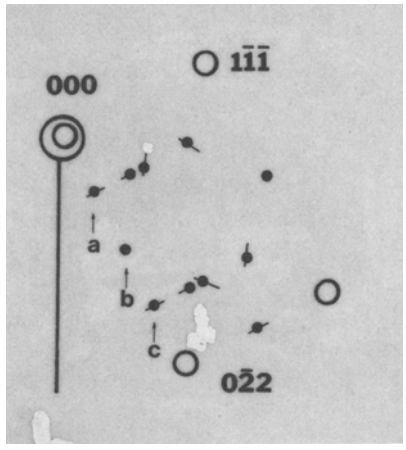

(c)

Fig 3—TEM micrograph of 68-T6 alloy: (*a*) BF showing T_1 in the needle-shape pattern (Z = [211]), (*b*) SAD of (a), and (*c*) key diagram of (b).

1.55 pct Li) in the T7 condition has less θ' and more T_1 than alloy 68-T6 (4.93 pct Cu, 1.19 pct Li), due to a higher lithium content and to the longer aging time of alloy 69-T7.

As evidence of the presence of the T_B ($Al_{7.5}Cu_4Li$) phase, satellite reflections were seen around the matrix reflections of both alloys, 68-T6 and 69-T7 (Figures 2, 3, and 5). These satellite spots are due to the double diffraction of 220_{T_B} and $20\bar{2}_{T_B}$, which are in near Bragg condition with Z = [001] and Z = [211], respectively. The same reflections were seen for I/M Al-2.7Li-2.3Cu-0.17Zr[15] and I/M X2020.[16] Even though, based on the diffraction patterns, the presence of T_B in these alloys was obvious, dark-field microscopy for the T_B phase was difficult at the peak strength conditions. However, the overaged condition, *i.e.*, T6 with additional aging at 335 °C (608 K) for 3 hours, revealed more strongly the existence of the T_1 and T_B phases. Figure 6, (a) and (b), shows bright-field and dark-field micrographs of T_B; they were obtained using $20\bar{2}$ of T_B around the matrix reflection $1\bar{1}1$ (Z = [211]) in Figure 6(c). It was frequently observed from alloys 68 and 69 that the dark-field image of θ' coincides with that of T_B. This supports the observation that the formation of T_B is due to the transformation of θ' in the presence of lithium.[6]

For the equilibrium T_B phase, the following orientational relationships were obtained by X-ray techniques:[6] $[100]_{T_B} \| [110]$, and $[001]_{T_B} \| [001]$. The T_B phase was reported to be disoriented by a rotation of 1 to 2 deg about the [100] axis.[6] An electron diffraction pattern analysis based on 220 reflections of the T_B phase revealed that the 68 alloy in the T6 condition has a slightly larger rotation angle (5 to 6 deg) than previous measurements showed. The 69-T7 alloy (overaged) showed 2 to 3 deg rotation. Also, the lattice parameters of T_B were shown to be different from 5.83 Å: a = 6.11 Å for the 68-T6 alloy and a = 5.96 Å for the 69-T7 alloy based on the diffraction analysis. These deviations are possibly attributed to the transition from an intermediate to the final stage of stable compound formation. Soviet work[17] reported that the T_B phase has the highest stability and hardness among the ternary compounds in the temperature range of 200 to 300 °C (473 to 573 K). The effect of T_B on the room temperature strength and deformation of the alloys has yet to be studied.

In general, there was no noticeable difference in second phase precipitation between the RS-PM 68 and I/M X2020 alloys.[16] Both alloys showed extensive co-precipitation of θ' and T_1 with an indication of the existence of T_B through the satellite reflections. Also, it was found from both alloys that δ' preciptation was insignificant. In contrast, it is interesting to note that the major precipitates in I/M Al-4.2 pct Cu-1.0 pct Li-0.5 pct Mn-0.2 pct Cd[9] are θ' and T_B. All three compositions belong to the region of Al + T_B in the ternary phase diagram at 500 °C (773 K).

Figure 7 shows the entirely different microstructure for alloy 70-T6 compared to those for alloys 68 and 69. The major precipitate in alloy 70-T6 (3.53 pct Cu, 2.79 pct Li) is the δ' phase, ranging in size from 100 to 200 Å. Figure 7(a) is a dark-field view obtained using one of the superlattice spots. Very small amount of the T_1 phase were found (see arrows in Figure 7(b)), and there was no evidence of T_B. Among the compounds in this alloy the T

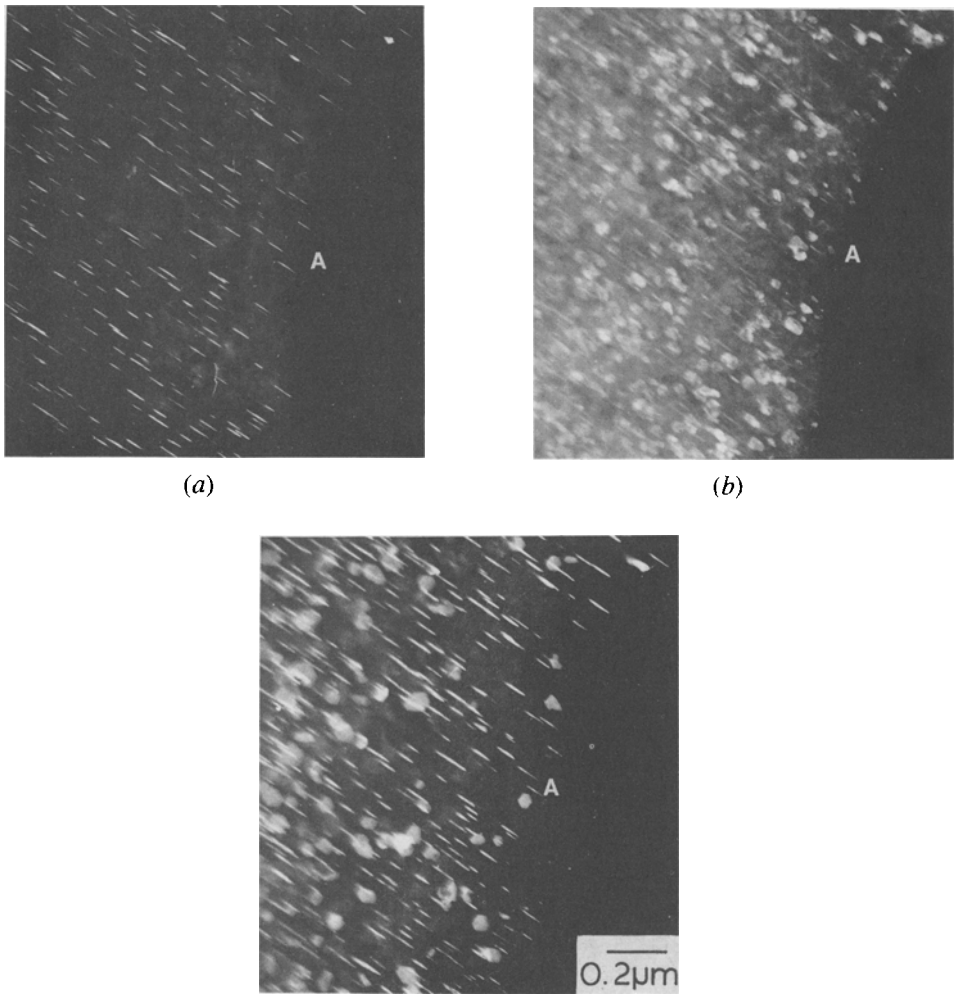

(*a*) (*b*) (*c*)

Fig. 4—TEM micrographs (DF) of 68-T6 alloy. The T_1 phase of (*a*) and (*c*), and the θ' phase of (*b*) are determined using reflections 'a', 'c', and 'b' in Fig. 3(c), respectively.

($Al_{20}Cu_2Mn_3$) phase was the most frequently found with a possibility of the presence of the T_2 phase in the 70 alloy.[5] It is highly possible for the 70 alloy to retain some T_1 and T_2 after solution heat treatment, based on the equilibrium phase diagram.

B. *Mechanical Properties*

Mechanical properties of each alloy were evaluated for peak aging conditions and are shown in Table II with representative TMT results. It is to be noted that mechanical properties reported in this study have limited accuracy due to the extrusion size and shape of these experimental alloys. As shown in Table II, strength and ductility values for the RS-PM alloys 68 and 69 are improved compared to I/M X2020 while the values for fracture toughness are lower. Higher strength levels in these alloys can be explained by the effective roles of oxides in inhibiting recrystallization and maintaining a refined microstructure.

Various exploratory TMT's did not provide improved properties compared to the simple aging heat treatments. Cold swaging (45 pct RA) of the 68 alloy, before solution heat treatment, resulted in a significant increase in ductility without any loss of strength. Based on the microstructures, this revealed that redistribution of the oxide stringers in the extruded bar during swaging is beneficial. Alloys 69 and 70, which have less severe oxide stringers than the 68 alloy, did not respond similarly for this TMT.

It has been reported that the presence of the δ' phase improves high cycle fatigue behavior (HCF).[19,20] It is also indicated that a refined grain structure obtained through rapid solidification powder processing provides increased resistance to fatigue crack initiation.[19,20,21] In Figure 8, all of the P/M Al-Cu-Li alloys show better S-N behvior, especially in HCF life, than do I/M X2020 and I/M 2024. Alloy 70-T6 shows the best fatigue performance among these alloys, whereas alloys 68-T6 and 69-T7 show similar but lower S-N fatigue resistance than does alloy 70-T6. The same observation was made based on fatigue crack growth rate (FCGR) measurements (Figure 9). Since the HCF region in the S-N test is controlled by fatigue crack initiation, the relatively higher ΔK_{Th} of alloy 70-T6 (6 ksi $\sqrt{\text{in}}$) than that of 68-T6 ($R = 0.33$) is in agreement with the high resistance of this alloy to fatigue crack initiation. The observed property differences are ascribed to the volume and nature of the precipitates and constituent particles, *i.e.*, δ' for 70-T6, and θ' and T_1 for alloys 68-T6 and 69-T7. Vasudévan and Suresh[22] also showed that ΔK_{Th} for I/M Al-Cu-Li alloys, for the same

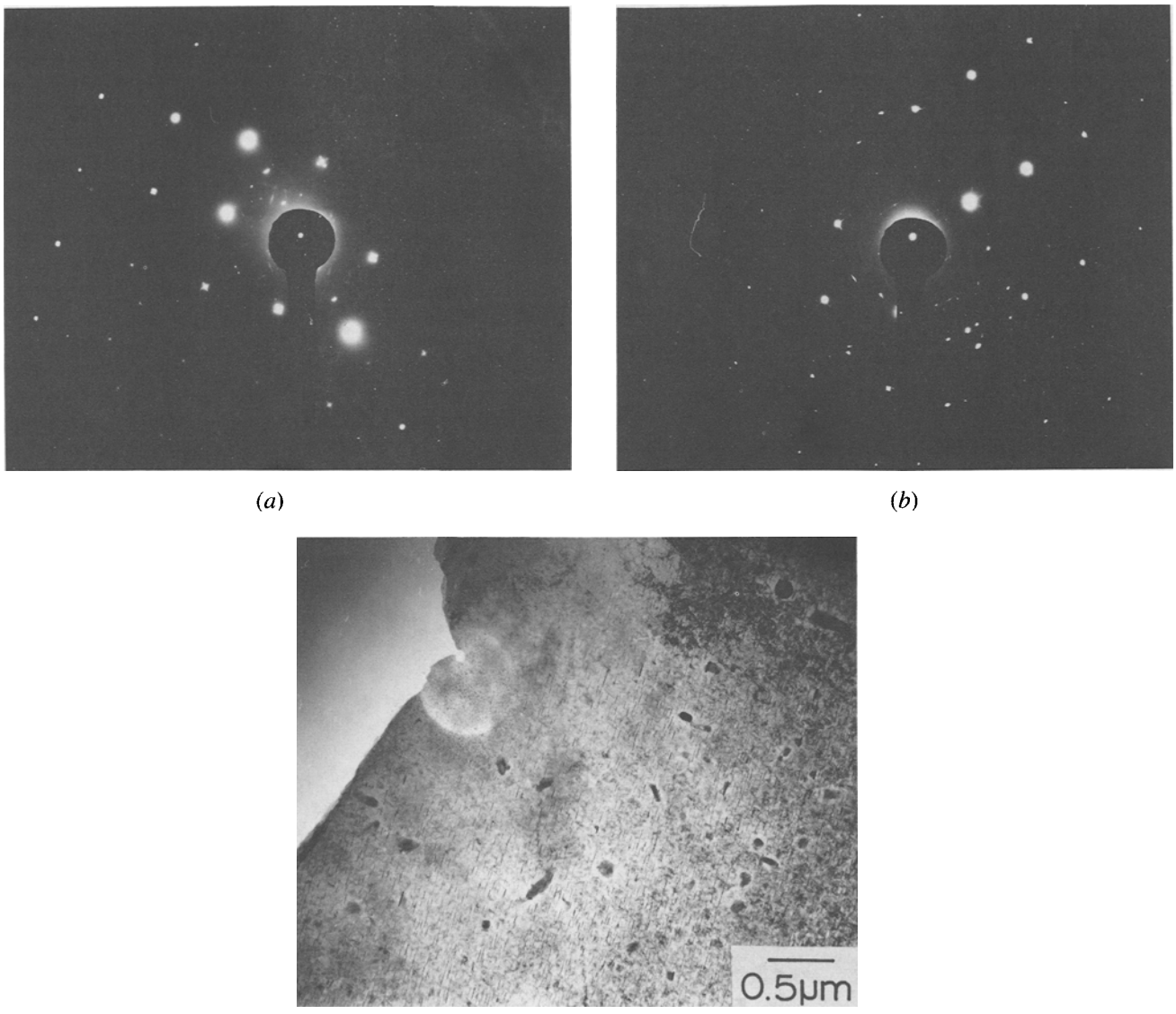

(*a*) (*b*) (*c*)

Fig. 5—TEM micrographs of 69-T7 alloy: (*a*) and (*b*) are SAD patterns with Z = [001] and [211], respectively, indicating the existence of θ' and T_1; (*c*) is a BF of T_1.

testing conditions (25 Hz, $R = 0.33$), increases with an increase in the Li/Cu ratio, supporting the useful role of δ' in crack initiation resistance. Figure 10 shows the fracture surfaces of 68-T6 and 70-T6 for an FCGR of 10^{-7} in/min ($R = 0.33$). The 70-T6 alloy shows dimpled fracture surfaces after all fracture tests that were made. The fracture is quite different from those of alloys 68 and 69, indicating that the δ' phase (and its volume fraction) plays an important role in the nature of the fracture.

In general, RS-PM Al-Cu-Li alloys showed inferior FCGR behavior to their I/M counterparts. The observed relatively high ΔK_{Th} of these alloys compared to those for I/M alloys in Figure 9 might not, however, be typical. As mentioned earlier, the size and the shape of the extrused bars for these alloys have shown noticeable effects on the measured mechanical properties, resulting in non-homogeneous mechanical properties across the extrusion cross-section in the L-T direction. It was noticed from this study that the center portion of the rectangular bar had 10 to 20 pct lower tensile property values than the edge portion, which experienced more deformation during the extrusion process. Severe tunneling observed during the precracking stage of these alloys could be due to the same reason. Among the microstructural differences, the grain size, dislocation density, and the oxide content and its distribution in RS-PM alloys are known to affect the FCGR significantly.[23,24] The rapid FCGR of RS-PM Al-Cu-Li alloys resulted in final failure at low stress intensity range values. The results of the compact tension tests in Table II show that the fracture toughness values of Al-Cu-Li alloys prepared by the RS-PM route are lower than those from I/M based alloys.

The fracture behavior of RS-PM X2020 alloys was demonstrated using interrupted tension tests; each specimen was cold stretched axially 2 to 4 pct after heat treatment and then mounted and polished longitudinally for observation. Figure 11(a) shows typical intercrystalline crack patterns for alloy 68-T6 involving grain boundaries and oxide stringers which are parallel to the loading axis. The TEM micrograph in

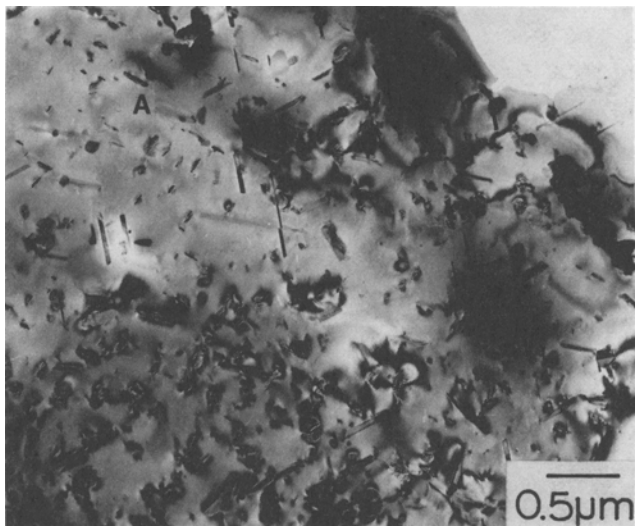

(a)

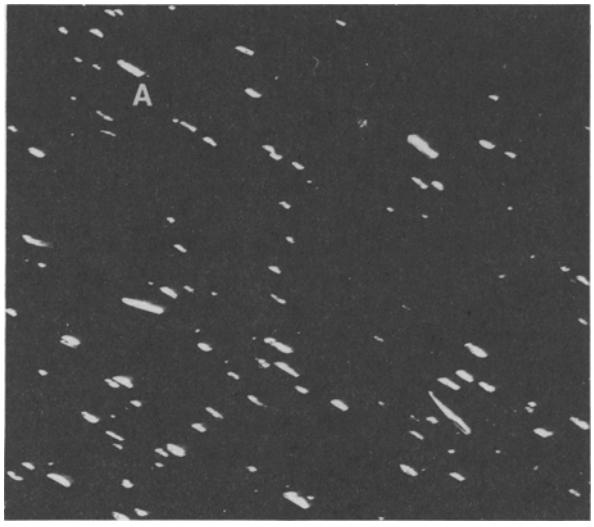

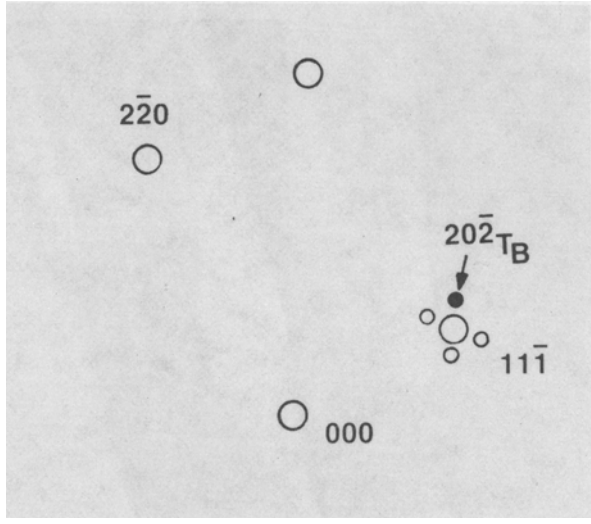

(b) (c)

Fig. 6—TEM micrographs of T_B obtained using 20$\bar{2}$ of T_B (Z = [211]) in the 68 alloy. T6 + aging at 335 °C (3 h)

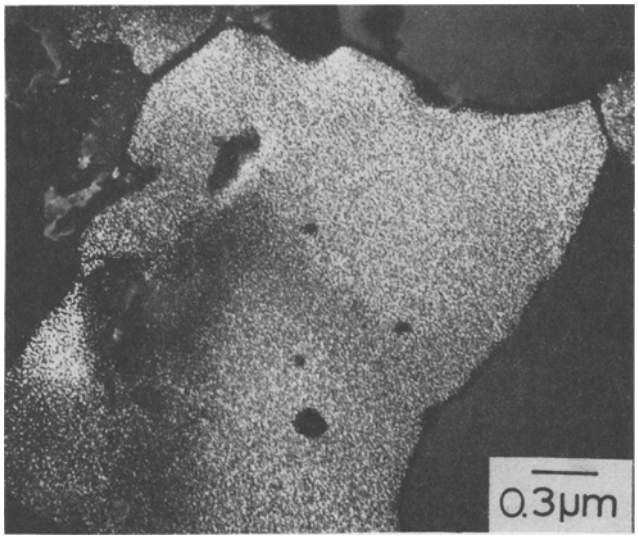

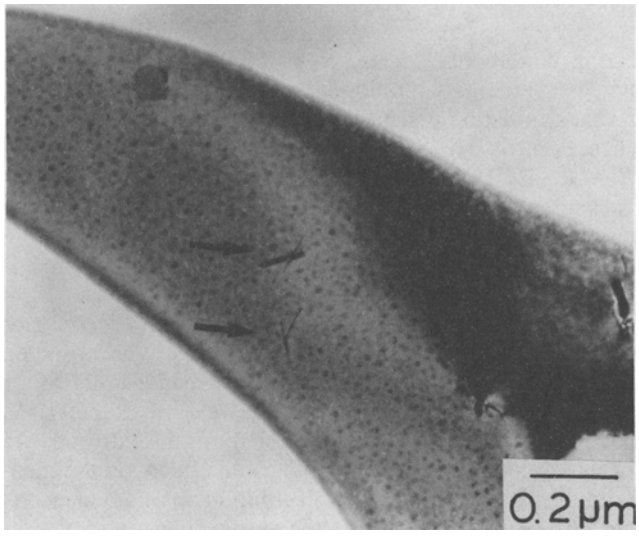

(a) (b)

Fig. 7—TEM micrographs of 70-T6 alloy: (*a*) is a DF of δ', and (*b*) is a BF of δ' with very little T_1 (arrows)

Table II. Room-Temperature Mechanical Properties†

Alloy	Heat Treatments	YS ksi	YS (MPa)	UTS ksi	UTS (MPa)	Elong. Pct	RA Pct	K_Q†† ksi$\sqrt{in}$	K_Q†† (MN/m$^{3/2}$)
2020-68-T6	ST*, age 448 K (16 h)	81.9	(565)	87.9	(606)	5.8	8.9	9.0 to 11.0	(9.9 to 12.1)
2020-68-T7	ST*, age 448 K (16 h), age 463 K (4 h)	74.5	(514)	80.6	(556)	6.3	15.5	—	
2020-68-T6 (CW)	CW (45 pct RA), ST*, age 448 K (16 h)	82.2	(567)	89.4	(617)	8.9	14.7	—	
2020-69-T6	ST*, age 448 K (14 h)	90.2	(622)	94.1	(649)	4.6	4.0		
2020-69-T7	ST*, age 448 K (14 h), age 463 K (4 h)	90.4	(623)	94.3	(650)	5.3	6.3	10.0 to 12.0	(11.0 to 13.2)
2020-69-T6 (CW)	CW (45 pct RA), ST*, age 448 K (14 h)	84.1	(580)	89.4	(617)	3.8	4.9	—	
2020-70-T6	ST**, age 433 K (22 h)	75.3	(519)	81.8	(504)	<3.0	—	10.0 to 12.0	(11.0 to 13.2)
2020-70-T7	ST**, age 433 K (22 h), age 463 K (3 h)	68.0	(469)	75.6	(521)	3.1	2.6	—	
2020-70-T6 (CW)	CW (26 pct RA), ST**, age 433 K (22 h)	36.0	(248)	62.2	(429)	9.3	6.2	—	
I/M X2020-T6	—	77.0	(531)	84.0	(580)	3.0	—	—	
I/M 7075-T6	—	73.0	(500)	83.0	(570)	11.0	—	25.0 to 27.0	(27.5 to 29.7)

†All tensile tests performed in longitudinal direction; results are average of at least two tests.
††Fracture toughness measured in L-T direction.
ST*, ST** = Solution treated at 798 K and 808 K, respectively, for 1 h, and water quenched.

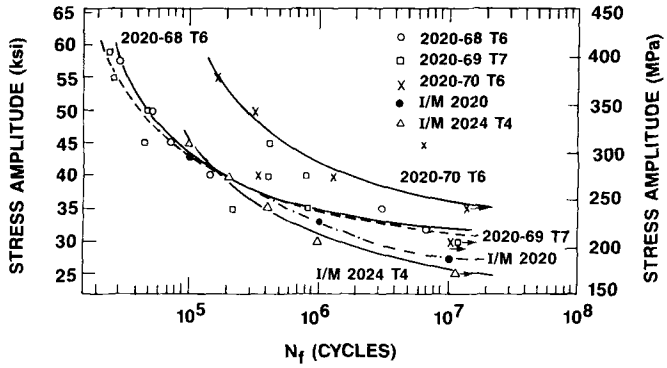

Fig. 8—Smooth bar S-N fatigue behavior of the alloys, compared with other aluminum alloys.[5]

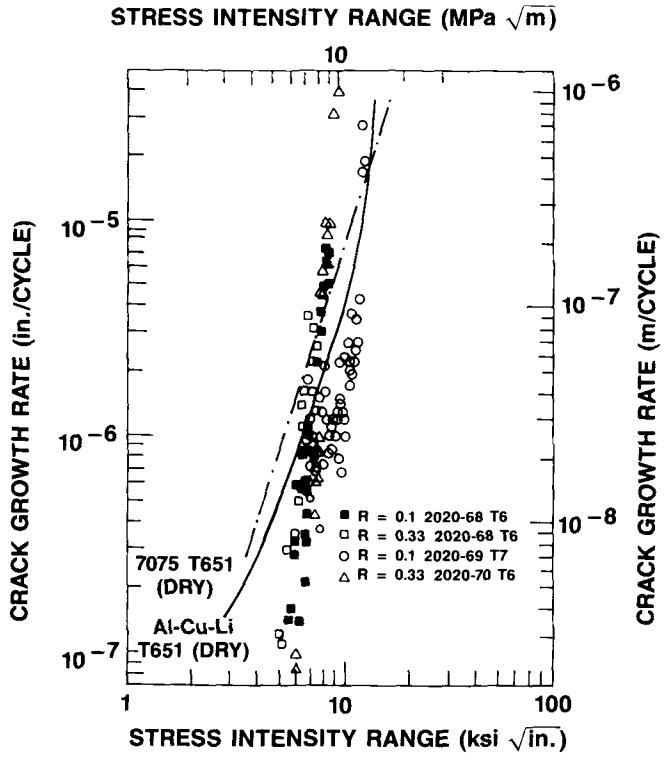

Fig. 9—Constant-load-amplitude fatigue crack growth behavior of the alloys, compared with I/M 7075-T651 and I/M X2020.[5]

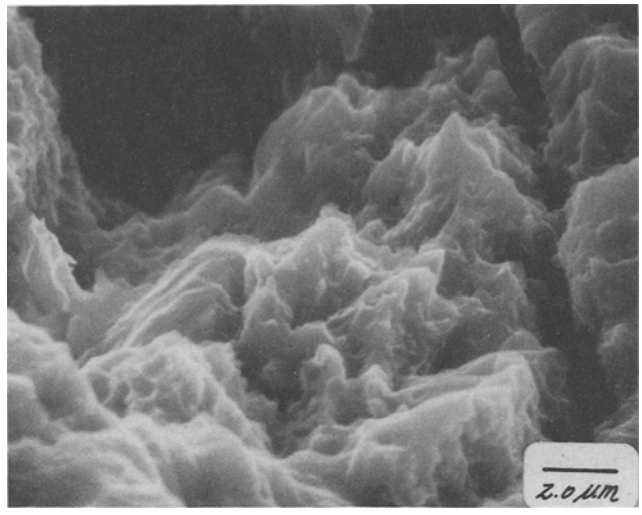

(*a*)

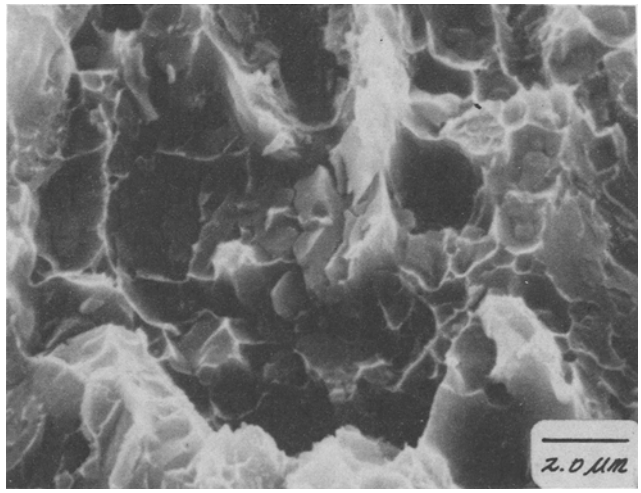

(*b*)

Fig. 10—Fracture surface of (*a*) 68-T6 and (*b*) 70-T6 for FCGR of 10^{-7} in/min at $R = 0.33$.

Figure 11(b) shows the location of oxides in the as-extruded structure. Local cracking in areas of high oxide concentration was observed to have taken place after relatively small amounts of cold stretching. The presence of PFZ's is an additional contribution to such early cracking. Another feature in the fracture of the 68 alloy with its heavy concentration of grain boundary oxides, is the large areal fraction of grain boundary facet-type fractures, 10 to 30 μm in size, regardless of heat treatment. Based on careful examination, it was concluded that these large facets are largely associated with previous powder poorly bonded powder boundaries. The 69-T7 alloy, which has fewer oxide stringers and a smaller grain size, showed no clear evidence of intergranular cracking even after a 4 pct stretch. The 70-T6 alloy also showed intergranular cracking along with fractured grain boundary precipitates. These precipitates are the T ($Al_{20}Mn_2Cu_3$) and possibly T_2 ($Al_6Cu\ Li_3$) phases based on limited EDXA results.[4] Overall results indicate that the fracture behavior patterns of RS-PM X2020 alloys were significantly influenced by processing details as well as by the secondary phases developed in the alloys.

IV. CONCLUSIONS

1. The phases which exist for the optimally aged conditions of RS-PM X2020 alloys, *i.e.*, the phases responsible for the strengthening and the microdeformation of the matrix, are θ', T_1, and T_B for alloys 68 and 69, and δ' for the 70 alloy. Tensile results showed clearly that the combination of the θ' and T_1 phases provides improved strength and ductility as compared to the δ' phase contribution.
2. It was found that the δ' phase is effective in delaying fatigue crack initiation and increasing ΔK_{Th} with an increase of the Li/Cu ratio.
3. The fracture behavior of RS-PM X2020 alloys is negatively influenced by the oxide content and oxide stringers as influenced by the consolidation step. The effect may be almost as important as the nature and distribution of the second phases in the alloy.

APPENDIX

Construction of electron diffraction patterns of the θ' (Al_2Cu) phase

Based on the modified Preston's structure[7,8] of the θ' phase, the location of atoms of the same kind per unit cell of θ' are determined: 000, $\frac{1}{2}\frac{1}{2}0$, $\frac{1}{2}\frac{1}{2}\frac{1}{2}$, $00\frac{1}{2}$ for aluminum atoms, $\frac{1}{2}0\frac{1}{4}$, $0\frac{1}{2}\frac{3}{4}$ for copper atoms. Using the structure factor, *i.e.*, $F_{hkl} = \sum_1^N f_n e^{2\pi i}\ (hu_n + kv_n + lw_n)$, which is obtained by simply adding together all the waves scattered by the individual atoms, various sets of planes, $\{hkl\}$, were examined for possible reflections. The results are summarized below:

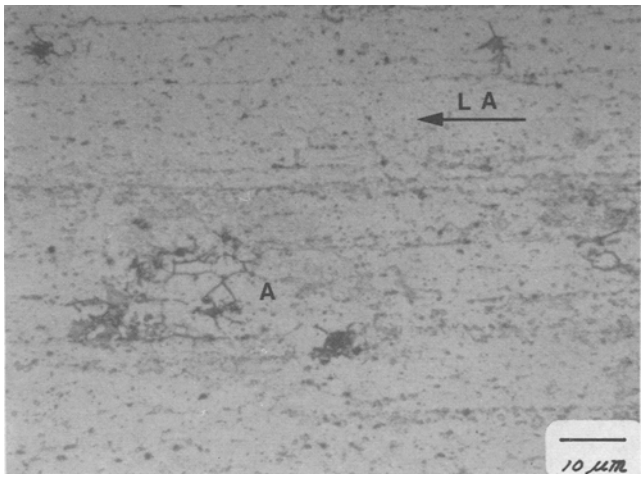

(*a*)

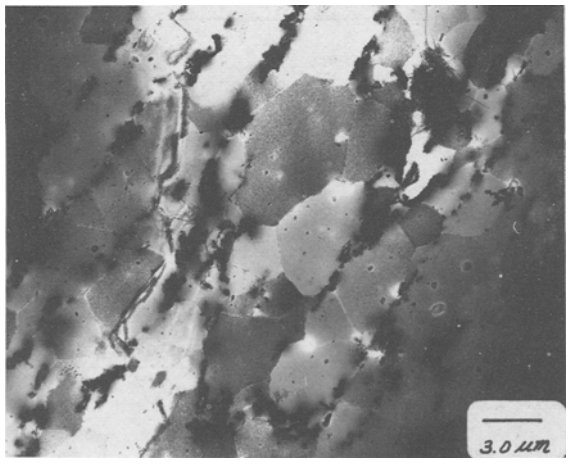

(*b*)

Fig 11—(*a*) Optical micrograph from a longitudinal section of 2 pct stretched 68-T6 alloy and (*b*) oxide distribution in the alloy

It is to be noted from the summary of the results that $F \neq 0$ as long as $h + k + l = 2n$ (n = any integer), implying that these sets of planes will result in reflections on the diffraction patterns. With this information, three different beam directions with respect to the thin disc-type θ' precipitate (these are equivalent to one incident beam direction with respect to the aluminum matrix) were considered in order to draw a possible diffraction pattern since the habit plane of θ' is {100}. Figure A, (a), (b), and (c), is due to $Z = [001]_{\theta'}$, $Z = [010]_{\theta'}$, and $Z = [100]_{\theta'}$, respectively. Each figure takes into account the double diffraction effect of electron beams for the many beam cases. In the case of $Z = [100]_{\theta'}$, as in Figure A(b), any one of the matrix reflections ($\bar{2}20$, 020, 220, $2\bar{2}0$, $0\bar{2}0$, and $\bar{2}\bar{2}0$) could be a source of the double diffraction. For $Z = [100]_{\theta'}$, any one of the matrix reflections such as $\bar{2}\bar{2}0$, $\bar{2}00$, $\bar{2}20$, $2\bar{2}0$, 200, and 220 will cause double diffraction. Figure A(d) illustrates a com-

Unmixed	all even	$l = 2m\ (m = 1,3,5\ldots)$	$F = 4f_{Al} - 2f_{Cu}$
		$l = 2n\ (n = 0,2,4\ldots)$	$F = 4f_{Al} + 2f_{Cu}$
	all odd	—	$F = 0$
Mixed	$h + k + l = 2n$	$l = 1,3,5\ldots$	$\lvert F\rvert^2 = 4f_{Cu}^2$
	$(n = 0,1,2,3\ldots)$	$l = 2m\ (n = 1,3,5\ldots)$	$F = 4f_{Al} + 2f_{Cu}$
		$l = 2n\ (n = 0,2,4\ldots)$	$F = 4f_{Al} - 2f_{Cu}$
	$h + k + l = 2n + 1$		
	$(n = 0,1,2,3\ldots)$	—	$F = 0$

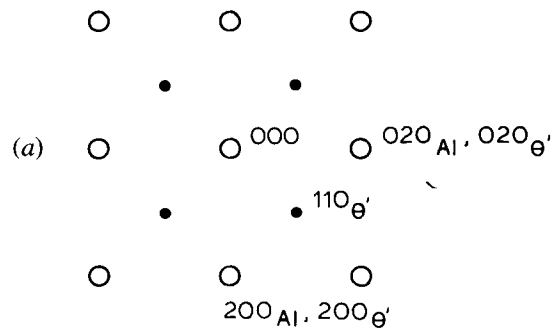

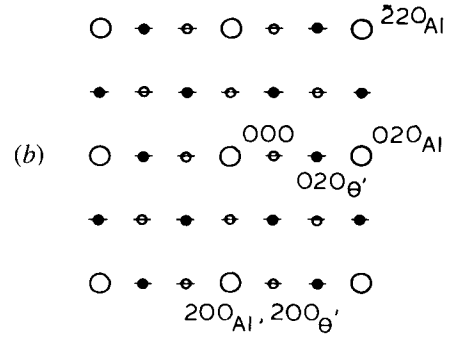

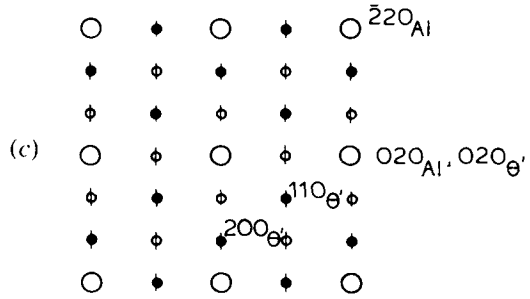

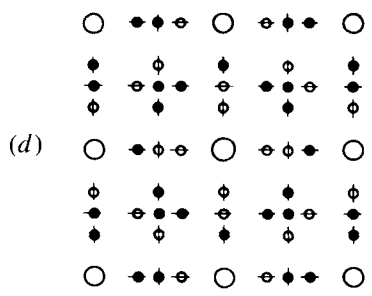

Fig. A—Partial diffraction patterns due to (*a*) Z = [001], (*b*) Z = [010], (*c*) Z = [100], and (*d*) superimposed diffraction patterns of (a), (b), and (c) ○: matrix, ●: precipitates, ○: double diffraction, –: streak.

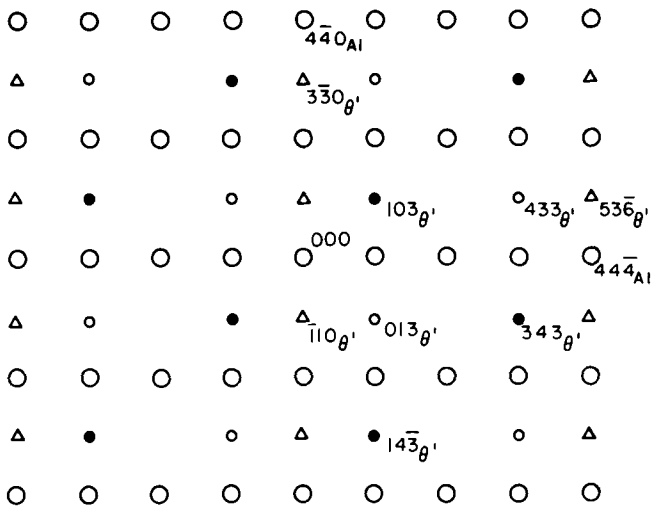

Fig. B—The constructed diffraction pattern of the θ' phase with Z = [112]. ○. matrix, ●: Z = [$\bar{6}32$], ○. [$3\bar{6}2$], △: Z = [334]

plete set of the diffraction patterns with $Z = [001]_{Al}$ which is consistent with TEM observations.

A similar method can be used to construct a diffraction pattern of the θ' phase with $Z = [112]_{Al}$. $Z = [112]_{Al}$ is almost equivalent to $Z = [\bar{6}32]_{\theta'}$, $Z = [3\bar{6}2]_{\theta'}$, and $Z = [334]_{\theta'}$, due to the habit plane of θ', {100}. Figure B is the diffraction pattern with $Z = [112]_{Al}$ without consideration of the double diffraction effect.

REFERENCES

1. J. W. Evancho Naval Air Development Center Contract No N62269-73-C-0219, June 1974.
2. T. H. Sanders, Jr. and E. S Balmuth: *Metal Prog.*, 1978, vol.114, pp 33-38.
3. E. S. Balmuth and R. Schmidt: *Proc of the 1st Int Aluminum-Lithium Conf.*, T H. Sanders, Jr. and E. A. Starke, Jr , eds., TMS-AIME, Warrendale, PA, 1981, pp. 69-88
4. S. Kang: Ph.D Thesis, MIT, Cambridge, MA, Feb. 1983.
5. S Kang and N. J. Grant: *Proc. of the 2nd Int Aluminum-Lithium Conf* , T. H. Sanders, Jr. and E A. Starke, Jr., eds., TMS-AIME, Warrendale, PA, 1984, pp. 469-84.
6. J. M. Silcock. *J. Inst. Metals*, 1959-60, vol. 88, pp. 357-64
7. G D. Preston: *Phil. Mag* , 1938, vol. 26, pp. 855-71.
8. J. M. Silcock, T. J. Heal, and H K Hardy: *J. Inst. Metals*, 1953-54, vol. 82, pp. 239-48.
9. K. Schneider and M Heimendahl. *Z Metallkde* , 1974, vol. 64, pp. 342-47.
10. G Thomas and M. J. Goringe: *Transmission Electron Microscopy of Materials*, John Wiley & Sons, New York, NY, 1979, pp. 88-90
11. P. Hirsh, A Howie, R B. Nicholson, D. W. Parshley, and M. J. Whelan: *Electron Microscopy of Thin Crystals*, Robert E. Krieger Publishing Co , New York, NY, 1977, pp. 324-27.
12. B Noble and G. E Thompson: *Metal Sci J* , 1972, vol 6, pp 167-74.
13. T. H Sanders, Jr., Naval Air Development Center Contract No. N62269-76-C-0271, June 14, 1979.
14. B. Noble and G. E. Thompson: *Metal Sci. J.*, 1971, vol. 5, pp. 114-20.
15. F. S. Lin, S B. Chakrabortty, and E A. Starke, Jr.: *Metall. Trans. A*, 1982, vol. 13A, pp. 401-10.
16. J. G. Rinker, M. Marek, and T. H. Sanders, Jr : *Proc. of the 2nd Int. Aluminum-Lithium Conf.*, T. H. Sanders, Jr. and E. A. Starke, Jr., eds., TMS-AIME, Warrendale, PA, 1984, pp. 597-626
17. Z. A. Sviderskaya and N. I. Turkina: *Izvest. Akad. Nauk. S.S.S R. Met. i Topl , Tekhn.*, 1962, vol. 1, pp. 151-55.
18. M. Holt and J. A Nock, Jr.: *Prod. Eng.*, 1960, vol. 31, pp. 38-41

19. K. K. Sankaran and N. J. Grant: *Mat. Sci. and Eng.*, 1980, vol. 44, pp. 213-27.
20. D. P. Voss: Eng. Doctor Thesis, Rheinish-Westfalischen Technischen Hochschule Aachen, Germany, Nov. 1979.
21. C. Y. Kung and M. E. Fine: *Metall. Trans. A*, 1979, vol. 10A, pp. 603-10.
22. A. K. Vasudévan and S. Suresh: *Metall. Trans. A*, 1985, vol. 16A, pp. 475-77
23 J. L. Robinson and C. J. Beever: *Metal. Sci. J* , 1973, vol. 7, pp. 153-59.
24. T. S. Kang and H. W. Liu: *Eng. Frac. Mech.*, 1974, vol. 6, pp. 631-38.